AGU PUBLICATIONS

JGR

Journal of Geophysical Research: Planets

RESEARCH ARTICLE
10.1002/2015JE004865

Key Points:
- Lunar magnetic anomalies deenergize ions via charge-separation electric fields
- Small-scale magnetic anomalies could produce minimagnetospheres
- Sputtering and space weathering could be reduced within a lunar magnetic anomaly

Correspondence to:
M. I. Zimmerman,
Michael.Zimmerman@jhuapl.edu

Citation:
Zimmerman, M. I., W. M. Farrell, and A. R. Poppe (2015), Kinetic simulations of kilometer-scale minimagnetosphere formation on the Moon, *J. Geophys. Res. Planets*, *120*, doi:10.1002/2015JE004865.

Received 19 JUN 2015
Accepted 12 OCT 2015
Accepted article online 15 OCT 2015

©2015. American Geophysical Union. All Rights Reserved.

Kinetic simulations of kilometer-scale minimagnetosphere formation on the Moon

M. I. Zimmerman[1], W. M. Farrell[2], and A. R. Poppe[3]

[1]The Johns Hopkins University Applied Physics Laboratory, Laurel, Maryland, USA, [2]NASA Goddard Space Flight Center, Greenbelt, Maryland, USA, [3]Space Sciences Laboratory, Berkeley, California, USA

Abstract Kinetic simulations are used to examine the solar wind's interaction with a 3 km wide region of strong crustal dipole magnetization on the Moon. In contrast with recent hybrid and implicit particle-in-cell simulations of magnetic anomalies that have aimed to resolve electric fields over several tens of kilometers, kinetic simulations reveal a much smaller scale regime in which magnetically driven ion-electron separation can generate a kV potential difference over a height of less than 200 m. The resulting electric field structure varies considerably between dawn and noon (when the solar wind flows, respectively, horizontally across the surface and vertically down from above) and is strong enough to reflect some ions back into space, consistent with spacecraft observations. Ion velocity and energy distributions are extracted near the surface and are used to derive maps of ion flux and impact energy, and the effects on sputtering and defect formation within the regolith are discussed. However, considerable uncertainty remains in how the surface ion flux evolves throughout a lunar day and how the plasma-surface-magnetic field interaction changes with respect to different magnetic topologies.

1. Introduction

Two of the leading factors responsible for generating electric fields and potentials on the Moon are direct solar wind bombardment and photoelectron emission. The former is controlled mostly by properties of the solar wind and its obstruction by topography, and the latter is a function of local illumination. The plasma environment thus varies dramatically between different areas of the Moon given respective variations in sunlight conditions, topography, and solar wind incidence [*Stubbs et al.,* 2014]. For example, the sunlit dayside produces a dense photoelectron cloud within the first few meters of the surface [*Poppe and Horányi*, 2010], the nightside is dominated mostly by energetic electrons penetrating the global lunar wake [*Halekas et al.,* 2005], and regions near the lunar terminator (where the solar wind flows almost horizontally with respect to the surface) can form miniature plasma wakes under the influence of local topography [*Farrell et al.,* 2010; *Zimmerman et al.,* 2011, 2012, 2013]. The interplanetary magnetic field (IMF) is important to the plasma dynamics and particle flow on larger scales; for instance, it causes some exospheric pickup ions to gyrate from the dayside around the Moon and into the nightside wake [*Halekas et al.,* 2012]. At scales less than a few kilometers, the interplanetary magnetic field plays a lesser role, which leaves the processes of surface charging and electric field creation relatively unaffected [*Zimmerman et al.,* 2013]. However, there is convincing evidence from spacecraft plasma measurements [*Lue et al.,* 2011; *Lin et al.,* 1998; *Kurata et al.,* 2005; *Halekas et al.,* 2008a, 2008b; *Hashimoto et al.,* 2010; *Saito et al.,* 2012], imaging of energetic neutral atoms [*Wieser et al.,* 2009, 2010], orbital magnetometer readings [*Hood et al.,* 1979, 2001; *Halekas et al.,* 2001; *Richmond and Hood,* 2008; *Mitchell et al.,* 2008; *Tsunakawa et al.,* 2010], and laboratory experiments [*Howes et al.,* 2015; *Wang et al.,* 2012, 2013; *Bamford et al.,* 2012] that localized regions of strong crustal magnetization, or "magnetic anomalies," can significantly alter the flow of solar wind.

Interestingly, many magnetic anomalies are colocated with intricate and contrasting patterns of optical brightness, called "lunar swirls." One hypothesis for formation of swirls is that the solar wind-anomaly interaction produces coherent electric fields that divert protons away from the surface and protect the areas below from ion-driven weathering that would otherwise darken the surface [*McCord et al.,* 2011]. If ion deenergization is significant enough, it could quench the local sputtered flux of neutrals feeding the global exosphere [*Poppe et al.,* 2014]. Magnetic anomalies thus represent a critical and unique scientific laboratory for studying the connections between space plasma physics, surface charging, surface weathering, and exospheric production.

In this paper electric field formation, surface charging, and ion deflection are studied in the presence of a dipolar magnetic anomaly using a kinetic plasma code. The region of strongest magnetic field is less than 2 km wide and about 500 m deep, in contrast with some of the more well known regional anomalies, including Airy and Reiner Gamma, which are tens of kilometers across. However, there are almost certainly more complicated magnetic field structures embedded within larger-scale anomalies, if the alternating albedo patterns found within lunar swirls are any indication of the near-surface magnetic field topology. By studying a smaller anomaly, we have been able to reveal new details of kinetic processes, including surface charging, that cannot be resolved by MHD simulations of larger anomalies.

A handful of plasma processes in lunar magnetic anomalies are thought to deflect some ions back into space, including charge-separation electric fields [*Neugebauer et al.,* 1972; *Halekas et al.,* 2011], magnetic mirroring of ions in cusp geometries [*Poppe et al.,* 2012; *Martínez-Sánchez and Ahedo,* 2011], and acceleration by MHD electric fields [*Jarvinen et al.,* 2014]. These are invoked in "solar wind standoff" theories that explain the formation of lunar swirls via deceleration or deflection of ions which reduces the energy available for ion-driven surface weathering. Other theories of swirl formation include selective motion of dust grains in the near-surface plasma environment [*Garrick-Bethell et al.*, 2011], increased photometric brightness due to collapse of the uppermost fragile layers of grains [*Pieters et al.,* 2014], and small-body impacts scouring away the topmost weathered layers of regolith and implanting a new crustal field [*Hood and Williams*, 1989; *Schultz and Srnka*, 1980]. However, there is a near-total lack of information on the magnetic field structure near the surface, despite a few in situ measurements made during the Apollo era [*Dyal et al*., 1970].

Modeling magnetic anomalies is complicated by the vast range of scales involved, from the anticipated few meters thick photoelectric layer [*Poppe and Horányi*, 2010; *Nitter et al.*, 1998] to crustal magnetic field regions that may cover tens of kilometers. Spacecraft measurements have suggested that when the solar wind flows horizontally past an anomaly, the resulting disturbance can extend hundreds to even thousands of kilometers downstream [*Futaana et al.,* 2003; *Saito et al.,* 2012; *Lue et al.,* 2011; *Halekas et al.,* 2008b]. Large-scale simulations have been able to resolve some of these features and have begun to address the importance of electric field formation due to MHD currents [*Jarvinen et al.,* 2014], the intriguing possibility of minimagnetosphere creation at lunar magnetic anomalies [*Harnett and Winglee,* 2002, 2003; *Deca et al.,* 2014], and ion reflection in magnetic cusp regions near the surface [*Poppe et al.,* 2012]. Recent laboratory experiments have also provided glimpses into the relevant plasma physics, showing that minimagnetospheres can indeed be created under some conditions [*Bamford et al.,* 2012] and that the plasma-magnetic field-surface interaction generates complicated electric potential structure due to a combination of kinetic effects [*Wang et al.,* 2012, 2013; *Howes et al.,* 2015].

However, there are numerous plasma physics issues that remain, such as fully characterizing the charge-separation processes that could occur in rapid magnetic field variations within tens to hundreds of meters of the surface, variations in illumination, latitude, and time of day, variable solar wind conditions and background IMF orientation, and the electrostatic influence of surface charging and photoemission on the near-surface plasma. In continuation of ongoing research into kinetic plasma physics at airless bodies, a two-dimensional kinetic plasma treecode [*Zimmerman et al.,* 2014] is used to study how the solar wind interacts with a strong, vertically aligned dipole magnetic field. The main focus of this work is on how the plasma-surface-magnetic field interaction produces electric fields that affect ion bombardment of the surface, in turn modulating space weathering and sputtering.

Section 2 provides a brief description of the simulation code and setup, which are similar to *Zimmerman et al.* [2014] except that a static background magnetic field has been added. In section 3, results are presented from simulations of a vertical magnetic dipole exposed to the drifting solar wind at sunrise and noon. At dawn the solar wind flows horizontally across the surface, forming a minimagnetosphere reminiscent of a large-scale magnetospheric shock. At noon the solar wind flows directly downward and electrons and photoelectrons tend to gather in the center of the anomaly, creating a strong electric field that is capable of reflecting jets of ions. In section 4 distributions of near-surface ion velocity, energy, and sputtered flux are extracted from the simulations and used to map out the yield of a sputtered neutral species. Concluding remarks are given in section 5, including a brief discussion of the implications for space weathering and swirl formation at the Moon.

2. Simulation Code and Setup

The two-spatial-dimension, three-velocity-component plasma treecode of *Zimmerman et al.* [2014] is used to model the solar wind's interaction with a small-scale but very strong crustal magnetic field at the Moon. The

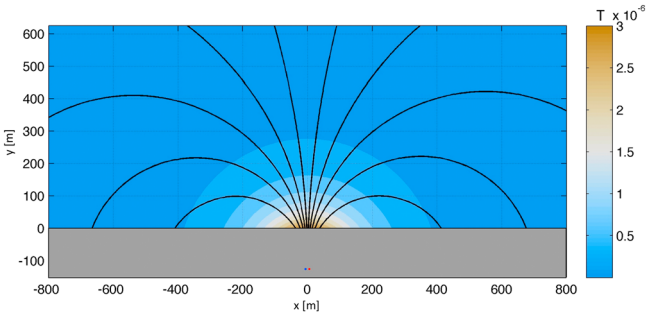

Figure 1. Magnetic field lines and strength for the dipole used in the simulations. The field is generated by two antiparallel currents at $x = \pm 5$ m, $y = -125$ m, shown as blue and red dots.

code is similar to a classical particle-in-cell code except that the grid-based electric potential solver has been replaced with an adaptive, tree-based electric field calculation, along the lines of *Christlieb et al.* [2006]. This enables regions of high particle density to be simulated at high spatial resolution while allowing for lower resolution where the plasma is more tenuous and the Debye length is larger. The treecode includes a careful accounting of charged particles accumulated and emitted by the surface, a self-consistent and high-fidelity boundary element method for computing electric fields due to surface charge, and a ray-casting technique to produce realistic illumination and photoemission conditions for arbitrary topography. The ability to specify a 2-D magnetic field has been added to the code, but diamagnetic effects are ignored: currents induced by the background field in these simulations are too small to create an appreciable diamagnetic field. The interplanetary magnetic field on the order of 4 nT is also ignored since the imposed crustal fields are 3 orders of magnitude larger, at least in the core of the domain.

Figure 1 shows the dipole magnetic field configuration used for all of the simulation runs, with the lunar surface at $y = 0$. Table 1 gives typical simulation parameters. The crustal field is produced by two antiparallel out-of-plane line currents at $x = \pm 5$ m buried 125 m below the surface, creating a vertically aligned dipole with maximum field strength 3 μT at $x = 0$ on the surface. This forms a vertical magnetic cusp, or region of field line convergence, just above the surface at $x = 0$, which is similar in character to the fully three-dimensional dipole field of a buried current loop. The two-dimensional dipole magnetic field is invariant to translations along the third dimension (i.e., the direction into the page in Figure 1). Far above the surface, this field is qualitatively similar to the measured structure of the Airy magnetic anomaly, i.e., having a magnetic cusp that is roughly uniform along one horizontal axis and converging along the other [cf. *Hemingway and Garrick-Bethell,* 2012, Figure 3c].

The choice of such a strong field with a source so close to the surface allows for a rapid-enough falloff in field strength that electrons respond quickly to the magnetic field before reaching the surface but ions remain unmagnetized. The ratio of the orbital strength of this dipole field to the maximum surface value is approximately $(d_{\text{source}}/(h_{\text{orbit}} + d_{\text{source}}))^3 \sim 10^{-7}$, where $d_{\text{source}} = 125$ m is the depth of the current source and $h_{\text{orbit}} = 30$ km is the orbital height. The simulated anomaly's magnetic field would be unmeasurable from orbit, but while the near-surface magnetic field within lunar anomalies is presently unconstrained, the present choice of field strength fits well within the existing orbital data. In comparison, recent large-scale models have assumed a magnetic dipole located tens of kilometers below the surface, giving a large region of weaker but more uniform magnetic field strength near the surface (1000 nT in *Deca et al.* [2014] and 100 nT in *Jarvinen et al.* [2014]).

For the boundary conditions of the treecode, Maxwellian distributions of electrons with thermal speed $v_{\text{the}} = 2 \times 10^6$ m s^{-1} and protons with thermal speed equal to the ion acoustic speed $c_s = 4.7 \times 10^4$ m s^{-1} are injected at the simulation edges with a drift velocity $v_{\text{sw}} = 4 \times 10^5$ m s^{-1} aligned to the direction of illumination, and the undisturbed solar wind concentration is $n_0 = 5 \times 10^6$ m^{-3} [cf. *Zimmerman et al.,* 2012]. At dawn the drift velocity is horizontal (along $+x$), and at noon it is downward (along $-y$). These parameters roughly amount to a 10 eV isothermal plasma in which the electrons are subsonic and the ions form a supersonic beam. For fully illuminated surface patches the level of photoelectron emission has a cosine dependence on the angle between the local surface normal and the direction of illumination. At dawn photoemission is inactive, and at noon it peaks with a given current density of 4 μA m^{-2}; under illumination, photoelectrons are emitted from the surface according to a Maxwellian distribution with thermal speed 6×10^5 m s^{-1} (corresponding roughly to a temperature of 1 eV) [*Willis et al.,* 1973; *Poppe and Horányi*, 2010].

The simulation box is 2.5 km × 1.0 km, ensuring (through trial and error) that solar wind electrons and photoelectrons from the surface are not artificially injected onto open field lines. Increasing the domain size to 5 km wide by 2.5 km high incurs a significant computational penalty but does not noticeably change the results.

Table 1. Simulation Parameters

Solar wind conditions	Concentration	n_0	5×10^6 m^{-3}
	Drift speed	v_{sw}	4×10^5 m s^{-1}
	Thermal speed	v_{the}	2×10^6 m s^{-1}
	Debye length	λ_{sw}	15 m
Photoelectron conditions (at noon)	Emission flux	j_{pe}	4 μA
	Thermal speed	v_{thpe}	6×10^5 m s^{-1}
	Surface Debye length	λ_{pe}	1.2 m
Magnetic properties at $R = 0$ m	Field strength	B_0	3.2 μT
	Undisturbed ion gyroradius	$m_p v_{sw}/q_e B_0$	1.4 km
	Undisturbed electron gyroradius	$m_e v_{the}/q_e B_0$	3.8 m
Magnetic properties at $R = 500$ m	Peak field strength	B_{500}^{max}	0.35 μT
	Minimum field strength	B_{500}^{min}	0.19 μT
	Undisturbed ion gyroradius	$m_p v_{sw}/q_e B_{500}$	11.9 km–22.0 km
	Undisturbed electron gyroradius	$m_e v_{the}/q_e B_{500}$	32 m–60 m

Any given simulation is run for 25 000 time steps of $\Delta t = 0.5$ μs (1/20 of the undisturbed photoelectron plasma period of about 10 μs) until a quasi-steady equilibrium is reached, and for analysis the results are time averaged onto a regular spatial grid over another 50 snapshots at a stride of 100 time steps.

3. Plasma Physics Environment

3.1. Lunar Dawn

At dawn the solar wind flows horizontally past the lunar surface and there is negligible illumination and photoemission. Time-averaged simulated particle concentrations, electric field, and electric potential for this case are shown in Figures 2 and 3. It is clear from Figure 2a that the electrons respond strongly to the presence of the magnetic field, within about 200 m from the origin, where the solar wind Debye length drops close to and below the local electron gyroradius (denoted by dashed lines in Figure 2a). Ions, whose density is shown in Figure 2b, have considerable inertia and remain unaffected by the magnetic field; this has been confirmed by test particle tracking with and without the magnetic field. Differences in how electrons and ions respond the magnetic field are crucial for understanding the resulting electric field structure: electrons become magnetized in the region of strongest magnetic field and are transported inward along field lines, while ions remain unmagnetized and respond only to charge-separation electric fields.

Figure 2a shows two regions where electrons visibly converge along the field lines. The upstream funnel, at about $x = 0$, is fed by electrons flowing in from the left and above. Farther downstream the electron density is depleted, since much of the solar wind has been deflected by the magnetic field; the backward moving part of this depleted population is the primary source for the converging funnel just above $x = 100$. Figure 2b shows a depletion in the ion concentration in the region of strongest magnetic field. In general, in the central anomaly, locations that are devoid of electrons in Figure 2a are filled with ions, as shown by the net charge concentration in Figure 2c. The resulting layers of adjacent but opposite charge create the electric field structure shown in Figure 3a, with peak strength in nonneutral regions near the surface and at the edges of the electron funnels. Ions entering the upstream lobe of the dipole (between $x = -400$ m and $x = 0$ m) create positive divergence in the electric field; the corresponding upward field component simultaneously accelerates the ions away from the surface and mixes them with the relatively undisturbed solar wind above the anomaly. This enhances the ion concentration (to about twice the background solar wind density) above and downstream of the anomaly, which is clearly visible in Figure 2b. Figure 2a shows that solar wind electrons respond by moving in to neutralizing the excess density of ions. Finally, downstream of the anomaly and near the surface, electrons and ions begin to refill the disturbed region through a wake-like process.

While the peak electric field in Figure 3a only reaches about 3 V m^{-1}, Figure 3b shows that integrating this field over the roughly 200 m deep anomaly produces a surface electric potential of $> +500$ V in the upstream lobe of the dipole, relative to the solar wind aloft. This is consistent with potential drops inferred from orbital measurements in larger-scale lunar magnetic anomalies [*Futaana et al.,* 2013]. For reference, the electric potential due to accumulated surface charge is shown in Figure 3c; the peak "surface charge" potential is two orders of

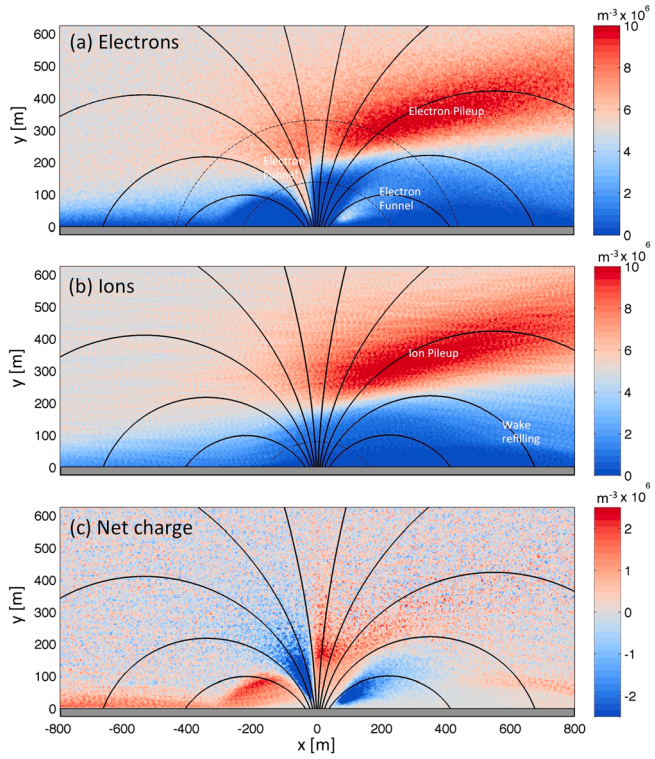

Figure 2. Concentration of (a) electrons, (b) ions, and (c) net charge in a vertical magnetic dipole, at dawn. The solar wind flows from left to right. The smaller and larger dashed curves in Figure 2a represent the surfaces at which $\lambda_{sw} = R_{le}$ and $\lambda_{sw} = 3R_{le}$, respectively, in the local magnetic field. The dashed line in Figure 2b represents the surface at which $L_i = 3R_{li}$.

magnitude lower than the total potential of Figure 3a; nonneutral space charge effects are obviously far more important to the total electric potential than surface charge accumulation.

3.2. Lunar Noon

Figure 4 shows the noontime interaction of the solar wind with the same dipole magnetic field, when the solar wind is flowing toward the surface from above. As in the dawn time case, Figure 4a shows that electrons tend to funnel and converge into the cusp region, but at noon the interaction is symmetric about the vertical axis since the solar wind flow vector is perfectly aligned with the magnetic dipole. The dipole lobes are magnetically inaccessible by solar wind electrons, which is consistent with reduced cross-field mobility. Photoemission peaks at noon, and Figure 4d shows that a dense population of photoelectrons is transported inward along the magnetic field lines from a wider area across the surface. Near the dipole axis they mix with solar wind electrons converging from above to create a very dense, negatively charged cloud just above the surface, cf. Figure 4e. A more detailed investigation of why electrons and photoelectrons are denied access to different regions of the dipole, based upon energy considerations [*Gurnett and Bhattacharjee,* 2005; *Draght,* 1965; *Störmer,* 1907], is outside the scope of this paper; rather, a quantification of ion-driven surface weathering is the main focus of this work. Finally, Figure 4c shows that ions outweigh the photoelectron density near the surface, leaving a net positive charge in the lobes.

The resulting electric field is shown in Figure 5a. To leading order the structure is simple: there is an inward and upward directed electric field pointing from the (positive) lobes to the more central (negative) cusp. The peak electric field is $>10\,\mathrm{V\,m^{-1}}$ near the origin, and integrating the roughly 4–5 $\mathrm{V\,m^{-1}}$ average field over the 200 m deep anomaly region produces an estimate of the $>+800$ V electric potential at the surface shown in Figure 5b. As in the dawn time case, the electric potential due to accumulated surface charge, Figure 5c, is an insignificant contribution to the total potential.

4. Ion Bombardment

4.1. Near-Surface Trajectories

The final goal of this work is to model how ion trajectories and their associated kinetic energy are affected by interaction with a magnetic anomaly. Figure 6 shows the results of tracing 1000 ion trajectories through the time-averaged electric fields of Figures 3 and 5. At dawn as the solar wind moves horizontally across the surface, an upward deflection of ions can be seen clearly in Figure 6a. Farther downstream, beyond the strongest part of the anomaly, ions slowly precipitate back toward the surface. At noon, Figure 6b shows that ions traveling down the cusp are accelerated inward (toward the dipole axis) and upward by the electric field; Figure 4b shows that there is a corresponding increase in ion concentration near the surface, and some portion of the ion population is reflected back into space, forming two oblique ion jets.

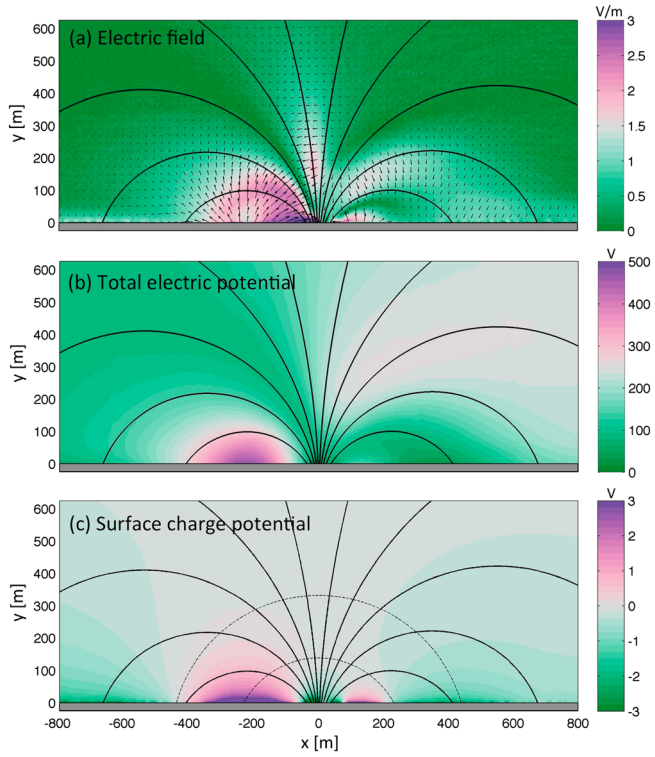

Figure 3. (a) Electric field magnitude and direction, (b) total electric potential, and (c) electric potential due to surface charge. Dashed lines in Figure 3c are the same as in Figure 2a.

4.2. Flux and Energy

Distributions of vertical ion velocity and total kinetic energy are shown in Figure 7. These have been reconstructed from all of the simulated ions within 15 m of the surface, accumulated over 50 snapshots of the position-velocity phase space of Figures 2b and 5b. In combination with the local ion concentration, the downward moving distribution (Figures 7a and 7d) can be integrated over velocity to produce the total ion bombardment rate (or flux) at the surface, while the kinetic energy distribution (Figures 7b and 7e) can be integrated to give an average energy available for sputtering/weathering per incident ion.

For the dawn time case, the velocity distribution of Figure 7a shows that the solar wind starts in a relatively undisturbed state (to the far left of the figure) and is dominated by thermal motion of ions toward the surface in the near-surface sheath. At about $x = -400$ m the ions begin to turn upward, and by about $x = -100$ m they have nearly all traveled out of the 15 m sampling domain. Figure 7b shows that in the undisturbed solar wind the total kinetic energy is dominated by the horizontal solar wind speed of 400 km/s, at about 1 keV. The kinetic energy decreases at the same location where the velocity distribution of Figure 7a begins to turn upward and the ions begin to decelerate horizontally in response to the large net positive charge in the upstream lobe; the energy subsequently increases as ions accelerate up and out of the thin near-surface sampling volume.

Much farther downstream ions return to the surface from aloft, first impacting at about $x = +500$ m. The magnetic anomaly acts like an obstruction to the solar wind, creating an effective plasma void that refills via wake formation. Figures 7a and 7b show the theoretical vertical velocity and total kinetic energy predicted by two-dimensional ambipolar wake theory, neglecting out-of-plane velocity components [*Farrell et al.,* 2010]:

$$v_\perp = c_s(1+\xi) \quad \text{with} \quad \xi = \frac{y_0 - y}{x - x_0}\frac{v_{sw}}{c_s} \tag{1}$$

$$\frac{KE_{tot}}{q_e} \sim \frac{m_p}{2q_e}\left(v_{sw}^2 + v_\perp^2\right) = \frac{m_p}{2q_e}\left(v_{sw}^2 + c_s^2(1+\xi)^2\right) \tag{2}$$

The initial wake formation point is chosen as $(x_0, y_0) = (200\text{ m}, 150\text{ m})$ which is a position just below the ion pileup in Figure 2b and above the region of strongest plasma interaction with the magnetic field. We believe that the agreement between the downstream ion velocity distribution of Figure 7a and the theoretical prediction of equation (1), along with the relative insensitivity of the prediction to changes in x_0 and y_0 up to 50 m in either direction, suggests the presence of an active wake refilling process. There is a second population of ions impacting the surface (with slightly smaller vertical speed) downstream of about $x = 800$ m, which remained close to the surface after passing through the anomaly.

At noon the velocity distribution and total kinetic energy distribution of Figures 7d and 7e show that undisturbed ions (far from the central interaction region) form a supersonic downward flowing beam with a velocity of vsw. In the dipole lobes ($100\text{ m} < |x| < 500$ m) ions are decelerated by the near-surface electric field, and there is an associated reduction in vertical velocity and total kinetic energy. Ions converge into the center

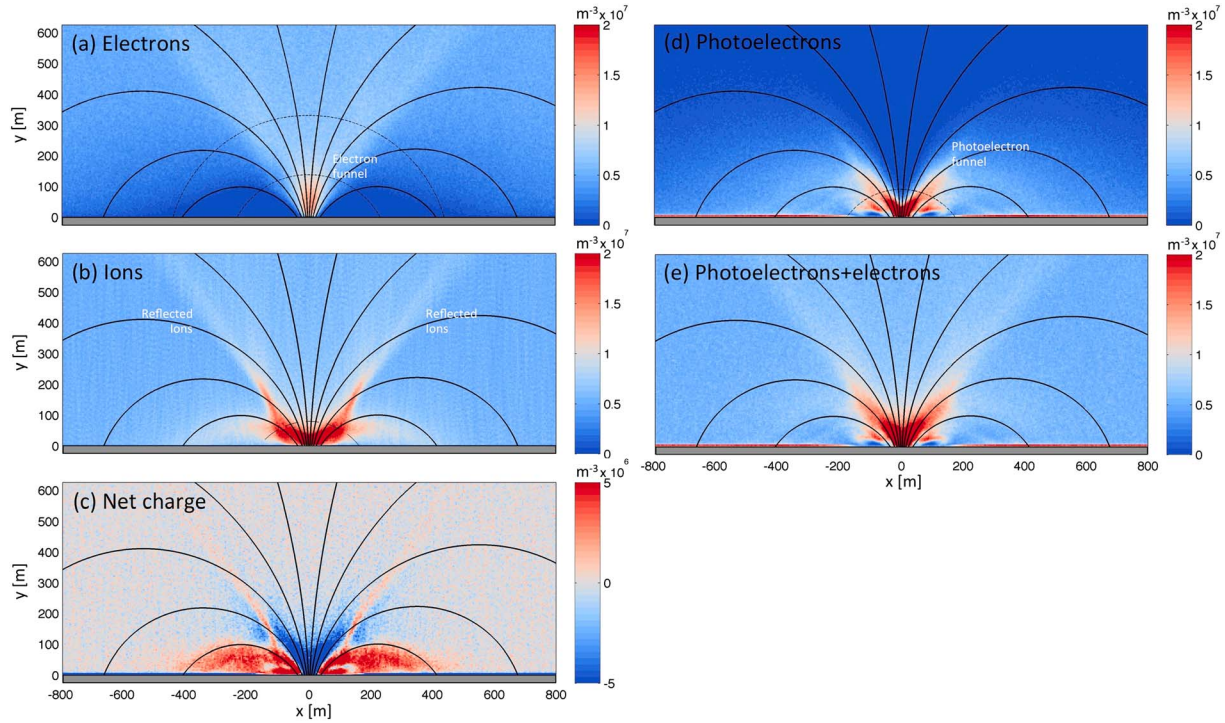

Figure 4. (a–c) As in Figure 2 except for downward solar wind flow at noon. Also shown are concentrations of (d) photoelectrons and (e) electrons plus photoelectrons.

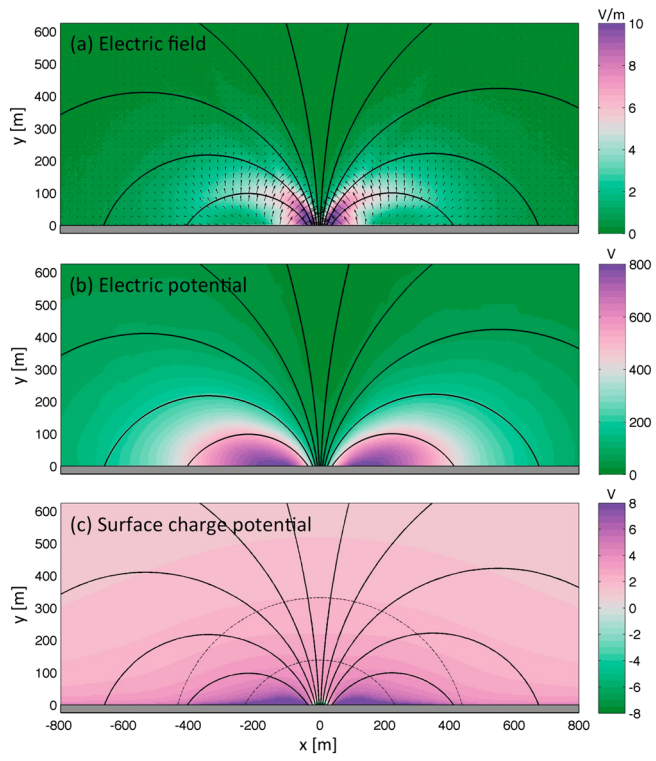

Figure 5. As in Figure 3 except for downward solar wind flow at noon. Dashed lines are the same as in Figure 4a.

of the dipole, forming a narrow spatial region of high concentration with a large spread in vertical velocity. Some of the upward moving reflected ions in the first 15 m above the surface have been captured in Figure 7, which are just beginning to form the upward moving jets to either side of the symmetry axis (cf. Figure 4b). There is also a pair of very tenuous horizontally ejected populations (at roughly $v_y = 0$); these ions have been turned sideways in the cusp before narrowly missing the surface and being driven sideways out of the anomaly. A handful of these ions are also visible in the particle tracking plot of Figure 6b.

4.3. Effects on Sputtering

The sputtering yield for oxygen from a KREEP (potassium, rare earth element, and phosphorus) lunar surface is approximately constant above the incident ion energy of 200 eV but falls off rapidly below this threshold, as modeled using the TRIM (TRansport of Ions in Matter) code [*Ziegler et al.,* 1996] with

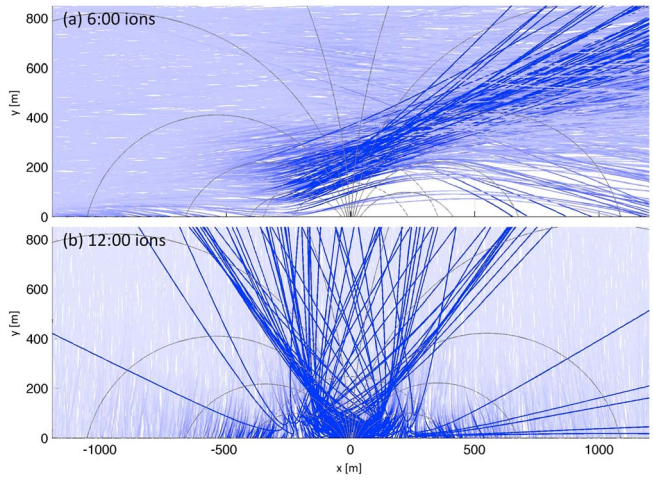

Figure 6. Ion trajectories traced in the electric and magnetic fields of (a) Figure 2 and (b) Figure 3. Deeper shades of blue correspond to greater ion deflections from each particle's original direction of flow.

the method of *Barghouty et al.* [2011]. We have chosen oxygen as a representative species for investigating the effects on neutral sputtering; the sputtering yield is about 0.025 oxygen atoms per incident solar wind proton above an incidence energy of 200 eV and approximately zero below [*Barghouty et al.*, 2011; *Starukhina*, 2003]. Figures 7c and 7f show the incident flux of ions (in blue), calculated as the average downward speed of the respective velocity distributions multiplied by near-surface number density. The sputtered flux of oxygen (shown in red) is calculated as the integral of dimensionless sputtering yield (per total energy) times the product of downward velocity and near-surface number density. The sputtered flux levels of Figures 7c and 7f are approximately 2 orders of magnitude less than the respective input fluxes, consistent with the ~0.025 constant yield value for all incident ions above 200 eV total kinetic energy. The sputtered flux levels also follow the shape of the input fluxes very closely; for the most part the incident energy stays above the 200 eV sputtering cutoff and the yield is effectively constant.

By its very nature, plasma sputtering creates defects in surface crystals by forming vacancies or holes in the lattice. As described by *Starukhina* [2006], such defects are ideal sites for enhanced trapping of implanted solar wind hydrogen. In essence, the solar wind plasma "pretreats" surfaces, making them more susceptible for retaining hydrogen and thus forming OH. In a defect-free surface, implanted H will quickly diffuse from the surface on time scales of less than a second [*Farrell et al.*, 2015]. In contrast, in defect-rich surfaces, there will be implantation sites

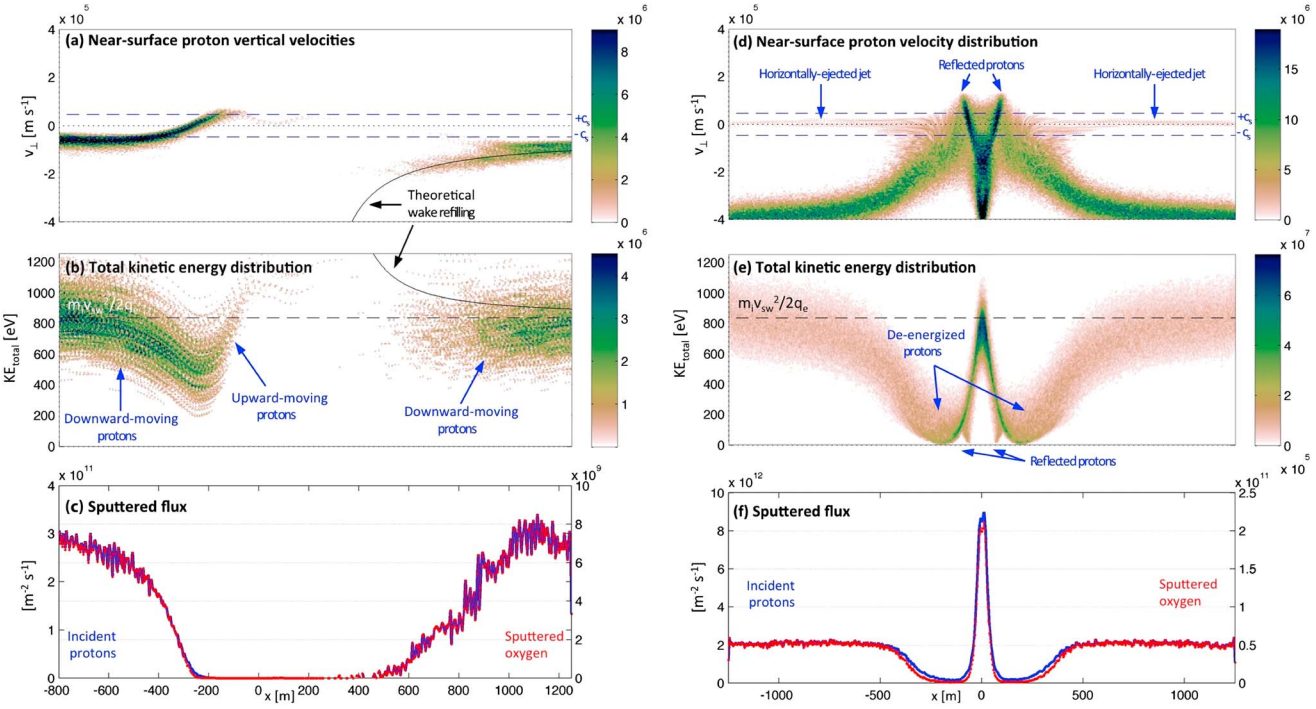

Figure 7. Distributions of ion (a, d) velocity and (b, e) energy in the first 15 m above the surface. Colors correspond to number of particles. (c, f) Incident and sputtered flux implied by the respective distributions of Figures 7a and 7b and Figures 7d and 7e.

at or near a defect that will allow trapping and long-term retention of the H (time scales over a lunation), to effectively form an OH bond. In examining Figure 7e, it is evident that the locations of solar wind ion entry and enhanced sputtering on open field lines are then also likely locations of retaining H at sputter-created defect sites and thus forming OH. In contrast, in the lobes/closed field lines, solar wind sputtering is vastly reduced and the defects needed to retain H are not as plentiful, giving rise to a lower OH content. The predicted lack of OH in the lobes is also consistent with the *Kramer et al.* [2011] result and likely results from having reduced sputtering and reduced surface density of vacancy-type defects in this protected regolith.

5. Concluding Remarks

The treecode simulations support previous assertions that crustal fields shield the surface from proton bombardment through creation of ambipolar electric fields [*Poppe et al.*, 2012; *Saito et al.,* 2012], and they also reveal the self-consistent ion fluxes and energy distributions impacting the surface, as well as providing a first detailed look at differences in the plasma environment between different times of day. At dawn and noon a minimagnetosphere is created in the first few hundred meters above the surface, which is a much smaller scale than analogous structures observed in MHD simulations [*Harnett and Winglee*, 2002, 2003; *Deca et al.,* 2014; *Jarvinen et al.*, 2014]. Strong electric fields tend to form where ions inertially separate from magnetically deflected electrons and photoelectrons, with associated potential drops on the order of the ion kinetic energy of about 1 keV. The resulting self-consistent electric field is sufficient to reflect some ions back into space and reduce the flux and energy of ions within the strongest part of the anomaly; these regions are most favorable for reducing the neutral sputtering yield.

Given that all lunar swirls are associated with magnetic anomalies on the Moon [*Blewett et al.,* 2011], it is tempting to conclude from this work that modulation of near-surface ion properties by a lunar magnetic anomaly will also directly affect long-term weathering of the surface. However, it is also important to consider that the daily time-integrated ion flux—not just any single snapshot of the flux at a given time of day—is required for a complete study of the solar wind's interaction with a lunar magnetic anomaly. It is not clear a priori which solar wind flow angles (i.e., which times of day) will dominate the flux of protons into the central converging field lines or if many times of day could provide equally important contributions to the time-integrated flux to the surface. Higher-order structure near the surface (quadrupoles, etc.) could also have considerable effects on the distribution of ions hitting the surface, which in turn will affect sputtering, space weathering, and defect formation.

Perhaps, the most important barrier to understanding lunar magnetic anomalies and their plasma physics connections with lunar swirls is that the strength and morphology of the relevant geomagnetic sources, and thus the near-surface magnetic field, is unconstrained. Large, deeply buried sources will tend to fall off more slowly just above the surface, creating larger-scale anomalies given sufficient magnetic field strength. Significant magnetization sources located just a few hundred meters under the surface (like in the present simulated cases) will create a strong near-surface field, possibly with a rapid gradient depending on the spatial distribution of magnetization. The present simulations show that a shallowly buried dipole magnetization can produce a minimagnetosphere on a scale of <1 km. A simple visual inspection of kilometer-scale albedo markings in some swirls (e.g., in Reiner Gamma, cf. the fine markings on the left side of Figure 4 of *Blewett et al.* [2007]) suggests that surface-darkening processes, possibly driven by the solar wind interacting with near-surface magnetic field gradients, could operate on similar scales.

Acknowledgments
We gratefully acknowledge funding for this work from the NASA Solar System Exploration Research Virtual Institute. For access to the simulation data used in this work, please contact the lead author by e-mail.

References

Bamford, R. A., B. Kellett, W. J. Bradford, C. Norberg, A. Thornton, K. J. Gibson, I. A. Crawford, L. Silva, L. Gargaté, and R. Bingham (2012), Phys. Rev. Lett. 109, 081101, Erratum, *Phys. Rev. Lett.*, *109*, 099902.

Barghouty, A. F., F. W. Meyer, P. R. Harris, and J. H. Adams Jr. (2011), Solar-wind protons and heavy ions sputtering of lunar surface materials, *Nucl. Instrum. Methods Phys. Res., Sect. B*, *269*, 1310–1315.

Blewett, D. T., B. R. Hawke, N. C. Richmond, and C. G. Hughes (2007), A magnetic anomaly associated with an albedo feature near Airy crater in the lunar nearside highlands, *Geophys. Res. Lett.*, *34*, L24206, doi:10.1029/2007GL031670.

Blewett, D. T., E. I. Coman, B. Hawke, J. J. Gillis-Davis, M. E. Purucker, and C. G. Hughes (2011), Lunar swirls: Examining crustal magnetic anomalies and space weathering trends, *J. Geophys. Res.*, *116*, E02002, doi:10.1029/2010JE003656.

Christlieb, A. J., R. Krasny, J. P. Verboncoeur, J. W. Emhoff, and I. D. Boyd (2006), Grid-free plasma simulation techniques, *IEEE Trans. Plasma Sci.*, *34*, 149.

Deca, J., A. Divin, G. Lapenta, B. Lembège, S. Markidis, and M. Horányi (2014), Phys. Rev. Lett. 112, 151102; Erratum, *Phys. Rev. Lett.*, *113*, 089902.

Draght, A. J. (1965), Trapped orbits in a magnetic dipole field, *Rev. Geophys.*, *3*, 255–298, doi:10.1029/RG003i002p00255.
Dyal, P., C. W. Parkin, and C. P. Sonett (1970), Apollo 12 magnetometer: Measurements of a steady magnetic field on the surface of the moon, *Science*, *196*, 762–764.
Farrell, W. M., T. J. Stubbs, J. S. Halekas, R. M. Killen, G. T. Delory, M. R. Collier, and R. R. Vondrak (2010), Anticipated electrical environment within permanently shadowed lunar craters, *J. Geophys. Res.*, *115*, E03004, doi:10.1029/2009JE003464.
Farrell, W. M., D. M. Hurley, and M. I. Zimmerman (2015), Solar wind implantation into lunar regolith: Hydrogen retention in a surface with defects, *Icarus*, *255*, 116–126, doi:10.1016/j.icarus.2014.09.014.
Futaana, Y., S. Machida, Y. Saito, A. Matsuoka, and H. Hayakawa (2003), Moon-related nonthermal ions observed by Nozomi: Species, sources, and generation mechanisms, *J. Geophys. Res.*, *108*(A1), 1025, doi:10.1029/2002JA009366.
Futaana, Y., S. Barabash, M. Wieser, C. Lue, P. Wurz, A. Vorburger, A. Bhardwaj, and K. Asamura (2013), Remote energetic neutral atom imaging of electric potential over a lunar magnetic anomaly, *Geophys. Res. Lett.*, *40*, 262–266, doi:10.1002/grl.50135.
Garrick-Bethell, I., J. W. Head III, and C. M. Pieters (2011), Spectral properties, magnetic fields, and dust transport at lunar swirls, *Icarus*, *212*(2), 480–492, doi:10.1016/j.icarus.2010.11.036.
Gurnett, D. A., and A. Bhattacharjee (2005), *Introduction to Plasma Physics With Space and Laboratory Applications*, Cambridge Univ. Press, Cambridge.
Halekas, J. S., D. L. Mitchell, R. P. Lin, S. Frey, L. L. Hood, M. H. Acuña, and A. B. Binder (2001), Mapping of crustal magnetic anomalies on the lunar near side by the Lunar Prospector electron reflectometer, *J. Geophys. Res.*, *106*, 27,841–27,852, doi:10.1029/2000JE001380.
Halekas, J. S., R. P. Lin, and D. L. Mitchell (2005), Large negative lunar surface potentials in sunlight and shadow, *Geophys. Res. Lett.*, *32*, L09102, doi:10.1029/2005GL022627.
Halekas, J. S., G. T. Delory, D. A. Brain, R. P. Lin, and D. L. Mitchell (2008a), Density cavity observed over a strong lunar crustal magnetic anomaly in the solar wind: A mini-magnetosphere?, *Planet. Space Sci.*, *56*, 941, doi:10.1016/j.pss.2008.01.008.
Halekas, J. S., D. A. Brain, R. P. Lin, and D. L. Mitchell (2008b), Solar wind interaction with lunar crustal magnetic anomalies, *Adv. Space Res.*, *41*, 1319, doi:10.1016/j.asr.2007.04.003.
Halekas, J. S., Y. Saito, G. T. Delory, and W. M. Farrell (2011), New views of the lunar plasma environment, *Planet. Space Sci.*, *59*, 1681–1694.
Halekas, J. S., A. R. Poppe, G. T. Delory, M. Sarantos, W. M. Farrell, V. Angelopoulos, and J. P. McFadden (2012), Lunar pickup ions observed by ARTEMIS: Spatial and temporal distribution and constraints on species and source locations, *J. Geophys. Res.*, *117*, E06006, doi:10.1029/2012JE004107.
Harnett, E. M., and R. M. Winglee (2002), 2.5D Particle and MHD simulations of mini-magnetospheres at the Moon, *J. Geophys. Res.*, *107*(A12), 1421, doi:10.1029/2002JA009241.
Harnett, E. M., and R. M. Winglee (2003), 2.5-D fluid simulations of the solar wind interacting with multiple dipoles on the surface of the Moon, *J. Geophys. Res.*, *108*(A2), 1088, doi:10.1029/2002JA009617.
Hashimoto, K., et al. (2010), Electrostatic solitary waves associated with magnetic anomalies and wake boundary of the Moon observed by KAGUYA, *Geophys. Res. Lett.*, *37*, L19204, doi:10.1029/2010GL044529.
Hemingway, D., and I. Garrick-Bethell (2012), Magnetic field direction and lunar swirl morphology: Insights from Airy and Reiner Gamma, *J. Geophys. Res.*, *117*, E10012, doi:10.1029/2012JE004165.
Hood, L. L., and C. R. Williams (1989), The lunar swirls: Distribution and possible origins, in *Lunar and Planetary Science Conference*, pp. 99, Houston, Tex.
Hood, L. L., P. J. Coleman Jr., C. T. Russell, and D. E. Wilhelms (1979), Lunar magnetic anomalies detected by the Apollo substatellite magnetometers, *Phys. Earth Planet. Inter.*, *20*, 291, doi:10.1016/0031-9201(79)90052-9.
Hood, L. L., A. Zakharian, J. Halekas, D. L. Mitchell, R. P. Lin, M. H. Acuña, and A. B. Binder (2001), Initial mapping and interpretation of lunar crustal magnetic anomalies using Lunar Prospector magnetometer data, *J. Geophys. Res.*, *106*, 27,825–27,839, doi:10.1029/2000JE001366.
Howes, C. T., X. Wang, J. Deca, and M. Horanyi (2015), Laboratory investigation of lunar surface electric potentials in magnetic anomaly regions, *Geophys. Res. Lett.*, *42*, 4280–4287, doi:10.1002/2015GL063943.
Jarvinen, R., M. Alho, E. Kallio, P. Wurz, S. Barabash, and Y. Futaana (2014), On vertical electric fields at lunar magnetic anomalies, *Geophys. Res. Lett.*, *41*, 2243–2249, doi:10.1002/2014GL059788.
Kramer, G. Y., et al. (2011), M3 spectral analysis of lunar swirls and the link between optical maturation and surface hydroxyl formation at magnetic anomalies, *J. Geophys. Res.*, *116*, E00G18, doi:10.1029/2010JE003729.
Kurata, M., H. Tsunakawa, Y. Saito, H. Shibuya, M. Matsushima, and H. Shimizu (2005), Mini-magnetosphere over the Reiner Gamma magnetic anomaly region on the Moon, *Geophys. Res. Lett.*, *32*, L24205, doi:10.1029/2005GL024097.
Lin, R. P., D. L. Mitchell, D. W. Curtis, K. A. Anderson, C. W. Carlson, J. McFadden, M. H. Acuna, L. L. Hood, and A. Binder (1998), Lunar surface magnetic fields and their interaction with the solar wind: Results from Lunar Prospector, *Science*, *281*, 1480, doi:10.1126/science.281.5382.1480.
Lue, C., Y. Futaana, S. Barabash, M. Wieser, M. Holmström, A. Bhardwaj, M. B. Dhanya, and P. Wurz (2011), Strong influence of lunar crustal fields on the solar wind flow, *Geophys. Res. Lett.*, *38*, L03202, doi:10.1029/2010GL046215.
Martínez-Sánchez, M., and E. Ahedo (2011), Magnetic mirror effects on a collisionless plasma in a convergent geometry, *Phys. Plasmas*, *18*, 033509, doi:10.1063/1.3554650.
McCord, T. B., L. A. Taylor, J.-P. Coombe, G. Kramer, C. M. Pieters, J. M. Sunshine, and R. N. Clark (2011), Sources and physical processes responsible for OH/H_2O in the lunar soil as revealed by the Moon Mineralogy Mapper (M^3), *J. Geophys. Res.*, *116*, E00G05, doi:10.1029/2010JE003711.
Mitchell, D. L., J. S. Halekas, R. P. Lin, S. Frey, L. L. Hood, M. H. Acuña, and A. Binder (2008), Global mapping of lunar crustal magnetic fields by Lunar Prospector, *Icarus*, *194*, 401, doi:10.1016/j.icarus.2007.10.027.
Neugebauer, M., C. W. Snyder, D. R. Clay, and B. E. Goldstein (1972), Solar wind observations on the lunar surface with the Apollo-12 ALSEP, *Planet. Space Sci.*, *20*, 1577–1591.
Nitter, T., O. Havnes, and F. Melandsø (1998), Levitation and dynamics of charged dust in the photoelectron sheath above surfaces in space, *J. Geophys. Res.*, *103*, 6605–6620, doi:10.1029/97JA03523.
Pieters, C. M., D. P. Moriarty III, and I. Garrick-Bethell (2014), Atypical regolith processes hold the key to enigmatic lunar swirls, Abstract 1408 presented at 45th Lunar and Planetary Science Conference.
Poppe, A., and M. Horányi (2010), Simulations of the photoelectron sheath and dust levitation on the lunar surface, *J. Geophys. Res.*, *115*, A08106, doi:10.1029/2010JA015286.
Poppe, A. R., J. S. Halekas, G. T. Delory, and W. M. Farrell (2012), Particle-in-cell simulations of the solar wind interaction with lunar crustal magnetic anomalies: Magnetic cusp regions, *J. Geophys. Res.*, *117*, A09105, doi:10.1029/2012JA017844.
Poppe, A. R., M. Sarantos, J. S. Halekas, G. T. Delory, Y. Saito, and M. Nishino (2014), Anisotropic solar wind sputtering of the lunar surface induced by crustal magnetic anomalies, *Geophys. Res. Lett.*, *41*, 4865–4872, doi:10.1002/2014GL060523.

Richmond, N. C., and L. L. Hood (2008), A preliminary global map of the vector lunar crustal magnetic field based on Lunar Prospector magnetometer data, *J. Geophys. Res.*, *113*, E02010, doi:10.1029/2007JE002933.

Saito, Y., M. N. Nishino, M. Fujimoto, T. Yamamoto, S. Yokota, H. Tsunakawa, H. Shibuya, M. Matsushima, H. Shimizu, and F. Takahashi (2012), Simultaneous observation of the electron acceleration and ion deceleration over lunar magnetic anomalies, *Earth Planets Space*, *64*, 83.

Schultz, P. H., and L. J. Srnka (1980), Cometary collisions on the Moon and Mercury, in *11th Lunar and Planetary Science Conference*, pp. 1009.

Starukhina, L. V. (2003), Computer simulation of sputtering of lunar regolith by solar wind protons: Contribution to change of surface composition and to hydrogen flux at the lunar poles, *Sol. Syst. Res.*, *37*, 36.

Starukhina, L. V. (2006), Polar regions of the Moon as a potential repository of solar-wind-implanted gases, *Adv. Space Res.*, *37*, 50–58, doi:10.1016/j.asr.2005.04.033.

Störmer, C. (1907), Sur des trajectoires des corpuscles electrisés dans l'éspace sous l' action du magnetisme terrestre, *Arch. Sci. Phys. Nat.*, *24*, 317–364.

Stubbs, T. J., W. M. Farrell, J. S. Halekas, J. K. Burchill, M. R. Collier, M. I. Zimmerman, R. R. Vondrak, G. T. Delory, and R. F. Pfaff (2014), Dependence of lunar surface charging on solar wind plasma conditions and solar irradiation, *Planet. Space Sci.*, *90*, 10–27.

Tsunakawa, H., H. Shibuya, F. Takahashi, H. Shimizu, M. Matsushima, A. Matsuoka, S. Nakazawa, H. Otake, and Y. Iijima (2010), Lunar magnetic field observation and initial global mapping of lunar magnetic anomalies by MAP-LMAG onboard SELENE (Kaguya), *Space Sci. Rev.*, *154*, 219.

Wang, X., M. Horányi, and S. Robertson (2012), Characteristics of a plasma sheath in a magnetic dipole field: Implications to the solar wind interaction with the lunar magnetic anomalies, *J. Geophys. Res.*, *117*, A06226, doi:10.1029/2012JA017635.

Wang, X., C. T. Howes, M. Horányi, and S. Robertson (2013), Electric potentials in magnetic dipole fields normal and oblique to a surface in plasma: Understanding the solar wind interaction with lunar magnetic anomalies, *Geophys. Res. Lett.*, *40*, 1686–1690, doi:10.1002/grl.50367.

Wieser, M., S. Barabash, Y. Futaana, M. Holmstrom, A. Bhardwaj, R. Sridharan, M. B. Dhanya, P. Wurz, A. Schaufelberger, and K. Asamura (2009), Extremely high reflection of solar wind protons as neutral hydrogen atoms from regolith in space, *Planet. Space Sci.*, *57*, 2132–2134.

Wieser, M., S. Barabash, Y. Futaana, M. Holmstrom, A. Bhardwaj, R. Sridharan, M. B. Dhanya, P. Wurz, A. Schaufelberger, and K. Asamura (2010), First observation of a mini-magnetosphere above a lunar magnetic anomaly using energetic neutral atoms, *Geophys. Res. Lett.*, *37*, L05103, doi:10.1029/2009GL041721.

Willis, R. F., M. Anderegg, B. Feuerbacher, and B. Fitton (1973), Photoemission and secondary electron emission from lunar surface material, in *Photon and Particle Interactions With Surfaces in Space*, pp. 389–401, Springer, Netherlands.

Ziegler, J. F., J. P. Biersack, and U. Littmark (1996), *The Stopping and Range of Ions in Solids*, Pergamon, New York.

Zimmerman, M. I., W. M. Farrell, T. J. Stubbs, J. S. Halekas, and T. L. Jackson (2011), Solar wind access to lunar polar craters: Feedback between surface charging and plasma expansion, *Geophys. Res. Lett.*, *38*, L19202, doi:10.1029/2011GL048880.

Zimmerman, M. I., T. L. Jackson, W. M. Farrell, and T. J. Stubbs (2012), Plasma wake simulations and object charging in a shadowed lunar crater during a solar storm, *J. Geophys. Res.*, *117*, E00K03, doi:10.1029/2012JE004094.

Zimmerman, M. I., W. M. Farrell, and T. J. Stubbs (2013), Recursive plasma wake formation on the Moon and its effect on polar volatiles, *Icarus*, *226*, 992, doi:10.1016/j.icarus.2013.06.013.

Zimmerman, M. I., W. M. Farrell, and A. R. Poppe (2014), Grid-free 2D plasma simulations of the complex interaction between the solar wind and small, near-Earth asteroids, *Icarus*, *238*, 77–85.